SAND2015-0938J

Parameter Uncertainty in LES of Channel Flow

C. Safta,[1, a)] M. Blaylock,[1] J. Templeton,[1] S. Domino,[2] K. Sargsyan,[1] and H.N. Najm[1]
[1)] *Sandia National Laboratories, Livermore, CA 94551*
[2)] *Sandia National Laboratories, Albuquerque, NM 87185*

(Dated: 16 January 2015)

PACS numbers: Valid PACS appear here
Keywords: Suggested keywords

I. INTRODUCTION

Large-eddy simulation (LES) is a method to compute the solutions to turbulent flows by resolving the larger flow features while modeling the smaller (sub-grid) scale fluctuations[1]. Mathematically, these two scales are separated by use of a low-pass filter, but most LES formulations do not account for the filtering operation explicitly. How to do so in the context of practical LES calculations has yet to be fully resolved, particularly because numerical errors can pollute the solution[2,3].

Several efforts have addressed this topic. Gullbrand and Chow[4] considered a dynamic reconstruction model to estimate the sub-grid stress (SGS) by approximately inverting an explicit filtering operator to compute part of it from the resolved turbulent flow field. As an alternative, Bose and Moin[5] considered directly modifying the SGS model with the filter width with the goal of providing "mesh-independent" LES results. Moser and co-workers[6,7] took a different strategy in which LES SGS model form and parameters were determined by applying linear stochastic estimation to channel flow in a technique known as optimal LES. Other approaches which explicitly bring information regarding the filter into the LES formulation involve boundary conditions. Previous studies have considered the effect of explicit filtering on boundary conditions for the Burgers' equation[8,9] and the Navier-Stokes equations[10,11], with the work of Bhattacharya *et al.*[11] being in the context of optimal LES.

The purpose of this paper is twofold: 1) we propose a framework for the estimation of uncertainties in the parameters for sub-grid scale turbulence models followed by a forward Uncertainty Quantification (UQ) study to examine the predictive capabilities of the LES approach given the calibrated set of parameters, and 2) we assess the feasibly of using directly filtered turbulence information to contribute to existing LES SGS models. Figure 1 shows a schematic of this framework, consisting of two intrinsically connected workflows, for *Parameter Estimation* and *Forward UQ*. The joint probability density for input parameters is estimated in a Bayesian framework. The Bayesian context provides a flexible framework to handle heterogeneous information and allows for sequential updates of posterior distributions as the prior information is revised. Both the model error ϵ_m and the measurement error ϵ_d can be embedded in the parameter estimation. The computational model, $\mathbf{f}$, is based on Sandia's FUEGO LES software suite. In the context of this work, we explore the predictive capabilities of $\mathbf{f}$ in a channel flow configuration, when employing the calibrated parameters for the k^{sgs} sub-grid scale model. We note that Bayesian estimation has been successfully used to infer model parameters within multiscale settings in other applications, such as molecular dynamics,[12,13] porous media flows,[14] and Carbon cycle models.[15,16]

There have been several prior efforts which used Bayesian[17] and other machine learning techniques to estimate uncertainties in turbulence simulations with particular emphasis on turbulence models. Decompositions of the RANS turbulent stress tensor have been considered as uncertain parameters and their effect on resulting RANS solutions has been quantified.[18–20] For example, the principal stress axes were computed and each perturbed to estimate the effect of structural uncertainty of turbulence models on flow realizations. The effects of uncertain boundary conditions have been examined using the Burgers' equation[21,22] and the Navier-Stokes equations.[23] Bayesian estimation of the effects of combustion models in LES has also been carried out,[24] while in cold flow isotropic turbulence, Lucor *et al.*[25] assumed a distribution for the constant in the Smagorinsky model following a Polynomial Chaos Expansion (PCE) which was sampled to compute the PCE of different scales of turbulent motion. Optimization-based calibration methods have also been applied to RANS models.[26] Other recent efforts have focused on using adjoint methods to assess model sensitivities.[29,30] A review article by Najm[28] provides a discussion on uncertainty quantification techniques, with emphasis on Polynomial Chaos expansions, in computational fluid dynamics.

Our interest in this work is to demonstrate a calibration strategy for LES SGS models and to provide means to propagate the uncertainty in the resulting models to quantities of interest. In this context, we plan to investigate how calibrated LES models fare in simulations with different physical parameters, numerical methods, and meshes. To the best of our knowledge, the first at-

[a)] Electronic mail: csafta@sandia.gov

tempt at deriving LES closures from resolved flow fields using machine learning strategies was the optimal LES formulation[7] which used linear stochastic estimation.[31] By using Bayesian inference, we can obtain model parameter uncertainties which enable the effect of imperfect calibration arising from sampling uncertainty and model form to be assessed on the LES flow field. In particular, we consider this propagation on a different flow field than the calibration study (i.e. isotropc flow vs. channel flow). Because the uncertainty in the ideal calibration process can be determined, this framework also enables us to start to quantify the uncertainties arising from other sources of error such as the mesh spacing and numerical method choice.

This paper is organized as follows. Section II provides a description of the LES formulation. Section III presents the Bayesian framework for model calibration. Specifically, the calibration data is discussed in Section III A followed by likelihood and prior constructions in Sections III B and III C. Posterior density results are presented in Section III D. Section IV describes propagation of uncertainties from calibrated model parameters to relevant quantities of interest in LES of channel flow. The channel flow setup is described in Section IV A, while Section IV B describes the Rosenblatt transformation employed to construct the PCE results presented in Section IV C. Section IV D presents probability densities for several quantities of interest for the channel flow studies. We end with conclusions in Section V. The methods employed in this paper are part of UQTk v3.0.[32]

II. LARGE EDDY SIMULATION

The LES field is formally defined as a low-pass filtered turbulent flow field, i.e.

$$\tilde{u}_i(\mathbf{x}) \equiv \int_\Omega u_i(\mathbf{y}) G(\mathbf{x}-\mathbf{y};\Delta)\, dV, \tag{1}$$

where u_i is the ith velocity component, $\tilde{u_i}$ is the filtered or LES ith velocity component, and G is a convolution kernel which preferentially removes small-scale energy from u_i. "Small-scales" are defined relative to the parametric dependence of G on a length scale Δ, denoted the filter width. If $\int_\Omega G\, dV = 1$ and it satisfies assumptions of isotropy, homogeneity, and continuous differentiability, the order of convolution and differentiation can be exchanged such that the equations governing the LES field as determined from the incompressible Navier-Stokes equations are

$$\frac{\rho\tilde{u}_i}{\partial t} + \frac{\partial \rho\tilde{u}_i\tilde{u}_j}{\partial x_j} = -\frac{\partial \tilde{P}}{\partial x} + \nu\frac{\partial^2\tilde{u}_i}{\partial x_j\partial x_j} + \frac{\partial \tau_{ij}}{\partial x_j}, \tag{2}$$

$$\frac{\partial \tilde{u}_j}{\partial x_j} = 0. \tag{3}$$

While similar to the Navier-Stokes equations, the LES equations differ through the inclusion of the SGS tensor

$$\tau_{ij} = \rho\tilde{u}_i\tilde{u}_j - \rho\widetilde{u_iu_j}. \tag{4}$$

Determining closure models for this term, particularly in complex engineering flows, remains an active area of research. We also note that when the assumptions on the filter are violated, as in wall-bounded flows, commutation error is incurred because differentiation and filtering no longer exactly commute.

Of relevance to our current effort, the SGS model not only expicitly depends on the convolution kernel G, but given the kernel and a turbulent flow field, it can be exactly determined. This mathematical relationship between the "true" flow field and the LES SGS tensor enables our goals of calibration, uncertainty propagation, and error assessment. Calibration can be achieved by filtering a direct numerical simulation (DNS) to exactly construct the terms present in the SGS model, from which model constants can be inferred. Given these constants, with quantified uncertainty, the error associated with the ideal LES model, based on the mathematics of continuous fields and filtering only, can be forward propagated in new solutions. The remaining error can be attributed to sources of uncertainty not present in the ideal LES.

A. k^{sgs} Turbulence Model

The transport equation for the LES transport model for the subgrid scale turbulent kinetic energy, k^{sgs}, is given by[33,34]

$$\int_V \frac{\bar{\rho}k^{sgs}}{\partial t}dv + \int_{\partial V}\bar{\rho}k^{sgs}\tilde{u_j}n_j ds = \int_{\partial V}\frac{\mu_k}{\sigma_k}\frac{\partial k^{sgs}}{\partial x_j}n_j ds + \int_V (P_k^{sgs} - D_k^{sgs})\, dv \tag{5}$$

The production and dissipation of turbulent kinetic energy, P_k^{sgs} and D_k^{sgs}, are given by

$$P_k^{sgs} = \left(2\mu_t\left(\tilde{S}_{ij} - \frac{1}{3}\tilde{S}_{kk}\delta_{ij}\right) - \frac{2}{3}\bar{\rho}k^{sgs}\delta_{ij}\right)\frac{\partial\tilde{u}_i}{\partial x_j} \tag{6}$$

and

$$D_k^{sgs} = C_\epsilon\frac{k^{sgs3/2}}{\Delta} \tag{7}$$

After expanding the parenthesis, the production term can be written as

$$P_k^{sgs} = 2\mu_t \left(\tilde{S}_{ij} \frac{\partial \tilde{u}_i}{\partial x_j} - \frac{1}{3} \left(\nabla \cdot \tilde{\mathbf{u}} \right)^2 \right) - \frac{2}{3} \bar{\rho} k^{sgs} \left(\nabla \cdot \tilde{\mathbf{u}} \right) \quad (8)$$

For incompressible flows, with $\nabla \cdot \tilde{\mathbf{u}} = 0$, the production term reduces to

$$P_k^{sgs} = 2\mu_t \tilde{S}_{ij} \frac{\partial \tilde{u}_i}{\partial x_j} \quad (9)$$

The filtered strain rate tensor is written as:

$$\tilde{S}_{ij} = \frac{1}{2} \left(\frac{\partial \tilde{u}_i}{\partial x_j} + \frac{\partial \tilde{u}_j}{\partial x_i} \right) \quad (10)$$

and the product $\tilde{S}_{ij} \frac{\partial \tilde{u}_i}{\partial x_j}$ can be further expanded as follows

$$\frac{1}{2} \sum_i \sum_j \left(\frac{\partial \tilde{u}_i}{\partial x_j} \right)^2 + \frac{1}{2} \sum_i \sum_j \frac{\partial \tilde{u}_j}{\partial x_i} \frac{\partial \tilde{u}_i}{\partial x_j} \quad (11)$$

The subgrid turbulent viscosity is modeled as

$$\mu_t = C_{\mu_\epsilon} \Delta k^{sgs\,1/2} \quad (12)$$

III. MODEL CALIBRATION

We employ a probabilistic approach, specifically a Bayesian framework, to compute posterior probabilities for the k^{sgs} model parameters, C_{μ_ϵ} and C_ϵ, introduced in Eqs. (7) and (12). In the Bayesian approach the posterior probability density for the model parameters is given by

$$p(\theta|\mathcal{D}) = L_{\mathcal{D}}(\theta) p(\theta) / p(\mathcal{D}) \quad (13)$$

Here, $\theta = \{C_{\mu_\epsilon}, C_\epsilon\}$ and $p(\theta)$ and $p(\theta|\mathcal{D})$ are the prior and posterior probability densities, respectively, for model parameters θ. These densities represent our knowledge about the values of C_{μ_ϵ} and C_ϵ before and after learning from the data $\mathcal{D}$. The likelihood function $L_{\mathcal{D}}(\theta) = p(\mathcal{D}|\theta)$ is the likelihood of the data $\mathcal{D}$ for a particular instance of θ. The denominator in Eq. (13), $p(\mathcal{D})$, is the "model evidence," and is not relevant for the calculations presented in this paper.

A. Calibration Data

For this study we employ the Johns Hopkins University (JHU) turbulence database[35,36] of forced isotropic turbulence in a periodic cube. Specifically, this dataset results from a DNS using 1024^3 grid nodes overlaying a cube with sides of length $L = 2\pi$. The Taylor-scale Reynolds number, Re_λ, for this simulation is approximately 433. The simulation covers a non-dimensional time range of 2.048 with solution files saved every 10 time steps, or 2×10^{-3}. For the current study we considered the DNS data at times $t = \{0, 0.1, 0.2, \ldots, 2.0\}$.

Filtered velocity values are computed from the DNS data using a top-hat filter of width Δ in all coordinate directions. The sub-grid scale kinetic energy is then computed as $k^{sgs} = \tilde{K} - K_{res}$, where $\tilde{K} = \widetilde{\frac{1}{2} u_i u_i}$ is the kinetic energy per unit mass and $K_{res} = \frac{1}{2} \tilde{u}_i \tilde{u}_i$ is its "resolved" component, computed using the filtered values.

The boundary integrals in Eq. (5) are statistically zero in a periodic configuration,

$$\int_{\partial V} \bar{\rho} k^{sgs} \tilde{u_j} n_j ds = \int_{\partial V} \frac{\mu_k}{\sigma_k} \frac{\partial k^{sgs}}{\partial x_j} n_j ds \equiv 0. \quad (14)$$

The remaining terms in Eq. (5) can be written in compact form as

$$f_k(t;\Delta) = C_{\mu_\epsilon} f_P(t;\Delta) - C_\epsilon f_D(t;\Delta) \quad (15)$$

where

$$f_k(t;\Delta) = \int_V \frac{\bar{\rho} k^{sgs}}{\partial t} dv, \quad f_D(t;\Delta) = \int_V \frac{k^{sgs\,3/2}}{\Delta} dv,$$
$$f_P(t;\Delta) = \int_V \Delta \sqrt{k^{sgs}} \tilde{S}_{ij} \frac{\partial \tilde{u}_i}{\partial x_j} dv \quad (16)$$

Spatial derivatives for terms f_P and f_D in Eq. (16) were computed at each time instant using second-order centered finite differences. For f_k, time derivatives were computed using centered finite differences using the data from solution files immediately adjacent to the corresponding time stamp. In addition to the dependence on time, the terms in Eq. (15) also depend on the filter width Δ.

Figure 2 shows slices though the DNS field in the left column. These slices correspond to planes perpendicular to the coordinate directions and centered at $x = y = z = \pi/2$. The top, middle, and bottom rows show the u, v, and w velocity components, respectively. The right column in this figure shows the corresponding filtered velocity components.

Figure 3 shows k^{sgs} in a $x-$const slice (left column) and $y-$const slice (right column), centered at the same point as in Fig. 2. The dependence of k^{sgs} on the filtered size is evident from this figure, as larger Δ values lead to more diffuse features for the filtered quantities.

Figure 4 shows the values of ratios f_k/f_D and f_P/f_D at several 0.1 time intervals. In this configuration, the production and dissipation terms are nearly proportional with a ratio that depends on the filter width. At the same time the time derivative of the overall sub-grid scale turbulent kinetic energy is smaller and varies around zero. This is to be expected in the forced isotropic turbulence configuration where energy is continuously injected to keep the total kinetic energy constant.

B. Likelihood Construction

In the Bayesian framework, the likelihood $L_{\mathcal{D}}(\theta)$ is the probability to observe the data $\mathcal{D}$ for an instance of the

model parameters θ. In this context, $\mathcal{D}$ consists of the values for f_k, f_P, and f_D, and the model is given by the right-hand side of Eq. (15). In order to construct the likelihood, using the data and this linear model, we first examine the degree of correlation, which is a measure of linear dependence, between several data components. We employ the Pearson correlation coefficient, ρ, for data pairs (f_k, f_P), (f_k, f_D), and (f_P, f_D). For all filter values Δ, the Pearson correlation coefficient values for the first two pairs, $\rho_{k,P}$ and $\rho_{k,D}$ are less than 0.4 in absolute value while $\rho_{P,D}$ (between production and dissipation data) are about 0.9. Based on these values we consider f_k to be uncorrelated from f_P and f_D, respectively. Further, we presume a bi-normal distribution for (f_P, f_D).

In general, the discrepancy between model predictions and the data can be formalized as[27]

$$f_k = \mathcal{M} + \epsilon_m + \epsilon_d. \tag{17}$$

Here, $\mathcal{M} = C_{\mu_\epsilon} f_P(t;\Delta) - C_\epsilon f_D(t;\Delta)$, ϵ_m is the model error, i.e. a consequence of the model only being an approximation of the true process, and ϵ_d is the data error, i.e. the discrepancy resulting from any imperfections in the measurement process. Under the above assumptions, the model $\mathcal{M}$ has a normal distrubution, $\mathcal{M} \sim N(C_{\mu_\epsilon} f_P - C_\epsilon f_D, \sigma^2_{\mathcal{M}})$, with

$$\sigma^2_{\mathcal{M}} = (C_{\mu_\epsilon}\sigma_P)^2 + 2C_{\mu_\epsilon} C_\epsilon \rho_{PD}\sigma_P\sigma_D + (C_\epsilon \sigma_D)^2 \tag{18}$$

and σ_P and σ_D are the standard deviations computed based on f_p and f_D data.

In the present context all data is gathered from numerical simulations, hence the data error is not considered in this study. The assignment of a statistical model structure for the model error ϵ_m is not straightforward and entails a significant degree of modeling.[27]

In this study we employ two modeling approaches to estimate ϵ_m. In the first approach we consider a normally distributed error model, with $\epsilon_m \sim N(0, \sigma^2)$. Under this assumtion the likelihood $L_{\mathcal{D}}(\theta)$ is approximated as a product of marginal densities at each time instant

$$L_{\mathcal{D}}(\theta) = \prod_{i=1}^{N_t} \frac{1}{\sqrt{2\pi}\sigma_i} \exp\left(-\frac{(f_{k,i} - C_{\mu_\epsilon} f_{P,i} + C_\epsilon f_{D,i})^2}{2(\sigma^2_{\mathcal{M}} + \sigma_i^2)}\right) \tag{19}$$

Here, the dependency on the filter width was dropped to simplify the notation. In this study we further assume the same standard deviation for all t_i with $i = 1, 2 \ldots, N_t$, $\sigma_i = \sigma$. The posterior distribution for σ will be estimated along with distributions for C_{μ_ϵ} and C_ϵ. One setback with this approach is that the model error term is now part of the calibrated model, i.e. the evolution of k^{sgs} is now governed by a right-hand side that includes a standard normal random variable in addition to the two terms shown in Eq. (15).

The second approach follows the works of Berliner[37] and Sargsyan *et al.*[27] who suggest to embedd the model error terms in the model components. By embedding the error model within the components themselves, the model predictions automatically contain all errors without the need to specify external error terms. We begin by parameterizing these model constants as

$$C_{\mu_\epsilon} = C_{\mu_\epsilon}(\boldsymbol{\alpha_1}),\ C_\epsilon = C_\epsilon(\boldsymbol{\alpha_2}) \tag{20}$$

where $\boldsymbol{\alpha_1}$ and $\boldsymbol{\alpha_2}$ are sets of parameters whose densities are yet to be determined. This effectively re-casts the calibration problem into one of estimating densities of θ such that the forward-propagated PDFs of C_{μ_ϵ} and C_ϵ, and subsequently of $C_{\mu_\epsilon} f_P - C_\epsilon f_D$, are consistent with the values of f_k.

For both approaches we presume that C_{μ_ϵ} and C_ϵ are random variables with finite variance and we will adopt a Polynomial Chaos expansion (PCE)[38,39] to represent these model constants. A brief description of PCE concept is presented below. For an in-depth description, the reader is referred to a series of publications on this topic.[38,40–42]

Consider a probability space $(\Omega, \mathfrak{S}, P)$, where Ω is a sample space, $\mathfrak{S}$ is a σ-algebra on Ω, and P is a probability measure on $(\Omega, \mathfrak{S})$. Let $\xi = \{\xi_1(\omega), \xi_2(\omega), \ldots\}$ be a set of independent standard random variables (RVs) on Ω. Then any RV $X : \Omega \to \mathbb{R}$ with finite variance, i.e. $X \in L^2(\Omega)$, can be represented as:

$$X(\omega) = \sum_{k=0}^{\infty} \alpha_k \Psi_k(\xi_1, \xi_2, \ldots) \tag{21}$$

where Ψ_k are multivariate polynomials, $\Psi_k(\xi_1, \xi_2, \ldots) = \Psi_k(\xi) = \Psi_{k_1}(\xi_1)\Psi_{k_2}(\xi_2)\ldots$ that are products of univariate polynomials. In a practical computational context, one truncates the PCE in both polynomial order p and dimensionality n. The number of terms in the resulting finite PCE

$$X(\omega) \approx \sum_{k=0}^{P} \alpha_k \Psi_k(\xi_1, \xi_2, \ldots, \xi_n) \tag{22}$$

and $P = (n+p)!/n!p!$.

Generalized Polynomial Chaos (GPC) expansions have been developed[42] using a broader class of orthogonal polynomials in the Askey scheme.[43] Each family of polynomials corresponds to a given choice of distribution for the ξ_i and is orthogonal with respect to the density of the vector of random variables ξ, i.e.

$$\langle \Psi_i \Psi_j \rangle = \int \Psi_i(\xi)\Psi_j(\xi) dP(\xi) = \delta_{ij}\langle \Psi_i^2 \rangle, \tag{23}$$

where δ_{ij} is Kronecker's delta. In general, popular choices for (ξ, Ψ) pairs are uniform RVs with Legendre polynomials or normal RVs with Hermite polynomials.

We employ Hermite-Gauss PCEs to represent C_{μ_ϵ} and C_ϵ as

$$C_{\mu_\epsilon} = \sum_k \alpha_{1,k}\Psi_k(\xi),\ C_\epsilon = \sum_k \alpha_{2,k}\Psi_k(\xi). \tag{24}$$

Here $\xi = \{\xi_1, \ldots, \xi_M\}$ is a vector of standard normal random variables, while $\Psi_k(\xi) = \Psi_{k_1}(\xi_1)\cdots\Psi_{k_M}(\xi_M)$ are multivariate Hermite polynomials, orthogonal with respect to the density of these standard normal random variables. To illustrate the functional form representation via PCEs we employ first order expansions for both parameters

$$\begin{aligned} C_{\mu_\epsilon} &= \alpha_{10} + \alpha_{11}\xi_1 \\ C_\epsilon &= \alpha_{20} + \alpha_{21}\xi_1 + \alpha_{22}\xi_2 \end{aligned} \tag{25}$$

A "triangular" form is adopted adopted above in order to avoid rotational symmetries. The likelihood, expressed as

$$L_{\mathcal{D}}(\boldsymbol{\alpha_1}, \boldsymbol{\alpha_2}) = p(\mathcal{D}|\boldsymbol{\alpha_1}, \boldsymbol{\alpha_2}), \tag{26}$$

is the multivariate density for $\mathcal{D} = \{(f_{k,i}, f_{P,i}, f_{D,i}), i = 1 \ldots N_t\}$. Generally, this multivariate density is hard to estimate accurately due to cost associated with numerical approaches such as the Kernel Density Estimate (KDE).[44,45] Instead, we approximate this multivariate density with a product of marginal densities corresponding to each data point

$$L_{\mathcal{D}}(\boldsymbol{\alpha_1}, \boldsymbol{\alpha_2}) = \prod_{i=1}^{N_t} p(\mathcal{D}_i|\boldsymbol{\alpha_1}, \boldsymbol{\alpha_2}), \tag{27}$$

To simplify the derivation below, we approximate $p(\mathcal{D}_i|\boldsymbol{\alpha_1}, \boldsymbol{\alpha_2})$ as $p(f_{k,i}|f_{P,i}, f_{D,i}, \boldsymbol{\alpha_1}, \boldsymbol{\alpha_2})$. Given that germs ξ_1 and ξ_2 are normal RV's and the model in Eq. (15) is linear, the marginal densities $p(f_{k,i}|f_{P,i}, f_{D,i}, \boldsymbol{\alpha_1}, \boldsymbol{\alpha_2})$ are normal densities with mean and variance, μ_i^* and σ_i^{*2} computed as

$$\begin{aligned} \mu_i^* &= \alpha_{10} f_{P,i} - \alpha_{20} f_{D,i} \\ \sigma_i^{*2} &= (\alpha_{11} f_{P,i} - \alpha_{21} f_{D,i})^2 + (\alpha_{22} f_{D,i})^2. \end{aligned} \tag{28}$$

In this paper we will employ acronyms PEM (presumed error model) for results based on the likelihood shown in Eq. (19) and EEM (embedded error model) for results based on the approach described in the later part of this section.

C. Prior Construction

A result of the present work is that the data presented in Section III A, in particular Fig. 4, does not contain sufficient information to constrain both model constants C_{μ_ϵ} and C_ϵ. The production and dissipation terms are nearly proportional to each other, while f_k, showing the overall change in k^{sgs}, is small and fluctuates around 0. While it is to be expected that the balance of subgrid kinetic energy should preferentially inform the ratio rather than the values of the two constants, it was not known *a priori* if the fluctuations in k^{sgs} would be sufficient to estimate the parameter values. It could be the case that the removal of the boundary flux terms is partially to blame, but it appears as though the time-scale of the sub-grid kinetic energy variation relative to the time-scale of the fluctuations in production and dissipation is also too small as in Fig. 4. With this observation, and in the absence of additional data, it is clear that one needs additional regularization to constrain the parameter estimation problem.

To this end we choose independent Gaussian priors, $\mathcal{N}(\mu^{pr}_{C_{\mu_\epsilon}}, \sigma^{pr^2}_{C_{\mu_\epsilon}})$ and $\mathcal{N}(\mu^{pr}_{C_\epsilon}, \sigma^{pr^2}_{C_\epsilon})$, centered at parameter values previously recommended in the turbulence modeling literature rather than Jeffreys (non-informative) priors. These values correspond to

$$\begin{aligned} \mu_1^{pr} &= (0.0845, 0.85)^{46} \\ \mu_2^{pr} &= (0.07, 1.05),^{33,34} \end{aligned} \tag{29}$$

respectively, for C_{μ_ϵ} and C_ϵ. For the classical approach, we explore a range of values for the marginal standard deviations for the prior densities, from $0.01 \ldots 0.04$ for C_{μ_ϵ}, and $0.1 \ldots 0.4$ for C_ϵ as follows

$$\sigma_1^{pr} = (0.04, 0.4),\ \sigma_2^{pr} = (0.02, 0.2),\ \sigma_3^{pr} = (0.01, 0.1) \tag{30}$$

For EEM we construct a prior that resembles the above formulation. In this approach the priors are set on the mean values of the two constants. Given the formulation proposed in Eq. (25), the mean values for $(C_{\mu_\epsilon}, C_\epsilon)$ are given by

$$\mu_{C_{\mu_\epsilon}} = \alpha_{10},\ \mu_{C_\epsilon} = \alpha_{20} \tag{31}$$

We adopt independent Gaussian priors for these means, with the same values as the ones mentioned above for the classical approach, in Eqs. 29 and 30. Further we truncate these densities so that

$$p^{pr}(\alpha_{10} \leq 0) = p^{pr}(\alpha_{20} \leq 0) = 0.$$

Additionally, we impose conditions on the other α coefficients to ensure only a small probability that C_{μ_ϵ} and C_ϵ are less than zero. We adopt a threshold value of 0.1% and impose

$$P(C_{\mu_\epsilon} < 0) < 10^{-3},\ \ P(C_\epsilon < 0) < 10^{-3} \tag{32}$$

For C_{μ_ϵ} this condition leads to

$$\alpha_{10} - 3|\alpha_{11}| > 0 \rightarrow p^{pr}(\alpha_{11}|\alpha_{10}) = \frac{\mathcal{H}(\alpha_{10} - 3|\alpha_{11}|)}{2\alpha_{10}/3}$$

where $\mathcal{H}$ is the Heaviside function. For C_ϵ, Eq. (32) leads to

$$p^{pr}(\alpha_{21}, \alpha_{22}|\alpha_{20}) = \frac{1}{4}\frac{\mathcal{H}(\alpha_{20} - 3\sqrt{\alpha_{21}^2 + \alpha_{22}^2})}{\pi\alpha_{20}^2/9}$$

The 1/4 factor in the above expression produces the correct normalization when considering only positive values

for α_{21} and α_{22}. The full prior for EEM is then written as

$$p^{pr}(\boldsymbol{\alpha_1}, \boldsymbol{\alpha_2}) = p^{pr}(\alpha_{10}) \times p^{pr}(\alpha_{11}|\alpha_{10}) \times p^{pr}(\alpha_{20}) \times p^{pr}(\alpha_{21}, \alpha_{22}|\alpha_{20}) \quad (33)$$

The denominators in the conditional prior densities $p^{pr}(\alpha_{11}|\alpha_{10})$ and $p^{pr}(\alpha_{21}, \alpha_{22}|\alpha_{20})$ can push both α_{10} and α_{20} towards the degenerate case $\alpha_{10} = \alpha_{20} = 0$. However, this is avoided by the truncated normal densities imposed above for these two model parameters.

D. Posterior Densities of k^{sgs} Parameters

A Markov Chain Monte Carlo (MCMC) algorithm is used to sample from the posterior probability density, $p(\theta|\mathcal{D})$ in Eq. (13). MCMC is a class of techniques that allows sampling from a probability density by constructing a Markov Chain that has the target density as its stationary distribution.[47] In particular, we employ an adaptive Metropolis algorithm,[48] which uses the covariance of the previously visited chain states to find better proposal distributions, allowing it to explore the posterior distribution in an efficient manner. We employ the Raftery-Lewis diagnostic[49] to determine when the MCMC samples converge to stationary posterior distributions. We also test the MCMC samples via the Effective Sample Size[50] (ESS) to determine if there is significant autocorrelation between chain samples.

We start with results from the PEM approach presented in the previous sections. In this context we presume that $\sigma_i = \sigma$ and we infer this value along with C_{μ_ϵ} and C_ϵ. In order to maintain positivity for the standard deviation we will actually work with $\log \sigma$, and use an improper prior for this parameter.

Table I presents the prior setup for the set of trials employed in this study. For each run, the filtered DNS data employed in the calibration was generated using several choices for the filter width $\Delta = \{L/64, L/32, L/16\}$. Henceforth, results corresponding to a certain prior setup will employ a subscript corresponding to the filter size used for the data, e.g. $\mathrm{R1}_3$ employs the setup for R1 with filter size $\Delta = L/16$, while $\mathrm{R3}_2$ employs the setup for R3 with filter size $\Delta = L/32$.

TABLE I: Setup for model calibration studies. μ^{pr}_{1-2} are defined in Eq. (29) while σ^{pr}_{1-3} are defined in Eq. (30).

Run	Prior mean	Prior St. Dev.
R1	μ_1^{pr}	σ_1^{pr}
R2	μ_2^{pr}	σ_1^{pr}
R3	μ_1^{pr}	σ_2^{pr}
R4	μ_2^{pr}	σ_2^{pr}
R5	μ_1^{pr}	σ_3^{pr}
R6	μ_2^{pr}	σ_3^{pr}

Figure 5 shows marginal PDFs for $\mathrm{R3}_2$. The 1D marginal densities are shown in the diagonal plots, while the contour plots show joint densities between C_{μ_ϵ}, C_ϵ, and σ, respectively. The narrow joint density for the pair $(C_{\mu_\epsilon}, C_\epsilon)$ indicate a strong dependence between these two parameters, specifically with respect to their ratio which is in line with the discussion in the previous subsection.

On the other hand, the joint posterior densities between these parameters and the standard deviation used in the likelihood construction, σ, suggests a weak dependency between the error term the model parameters. The marginal PDF results based on other filter sizes and/or other prior specifications (i.e. mean value, standard deviation) are qualitatively similar to results shown in Fig. 5.

Figure 6 shows marginal posterior densities corresponding to parameters α_{ij} that define the models for C_{μ_ϵ} and C_ϵ in the EEM aproach. These densities were computed via KDE using 5×10^6 MCMC samples. Parameters α_{10} and α_{20} that correspond to the means of C_{μ_ϵ} and C_ϵ exhibit a joint distribution that is very similar to the joint distribution for these model constants observed in Fig. 5 for the PEM approach. The first order coefficients, α_{11} and α_{21}, corresponding to the first random variable, ξ_1, also exhibit a strong dependency. Other 2D joint distributions show little correlations between parameters α_{ij}. It should be also noted that conditions in Eq. (32) are reflected in some sharp boundaries observed for several 2D joint posterior densities.

Figure 7 compares posterior densities for C_{μ_ϵ} and C_ϵ obtained with the PEM and EEM approaches. Each set of results is represented with five equally spaced contours. The results in this figure, corresponding to the three filter widths for R3, show consistently narrower densities for the PEM approach compared to EEM. For the former approach, the posterior densities for the model parameters only partially explain the discrepancy between the model and the data, the remaining contribution manifesting through the error terms in Eq. (17). For the EEM approach, the model parameters are parameterized such that the output density is consistent to the spread in the data. For this approach the discrepancy between the model, in this case the k^{sgs} sub-grid model, and the data is completely folded into the density of C_{μ_ϵ} and C_ϵ.

Figures 8 and 9 show the posterior mean and standard deviations based on marginal posteriors for C_{μ_ϵ} and C_ϵ, respectively. These figures show results for the three filter widths, discussed in Section III A, and prior model specifications, provided in Table I. For the PEM approach, the marginal posterior standard deviation for C_{μ_ϵ}, $\sigma^{Ps}_{C_{\mu_\epsilon}}$ in Figs. 8a and 8b, is about half compared to the corresponding prior density, while for C_ϵ, $\sigma^{Ps}_{C_\epsilon}$ in Figs. 9a and 9b, the discrepancy between prior and marginal posterior standard deviations is smaller. The corresponding results for the EEM approach, in Figs. 8(c,d) and 9(c,d), show larger marginal standard deviations for both model constants compared to PEM. The posterior means $\mu^{Ps}_{C_{\mu_\epsilon}}$ and $\mu^{Ps}_{C_\epsilon}$ are less impacted by the prior widths than the posterior standard deviations. The PEM and EEM results corresponding to runs R1 and R2 are similar, while for smaller prior widths, i.e. runs R3 through R6, the

posterior means for both model parameters are smaller for EEM compared to PEM.

In order to measure the degree of dependence between C_{μ_ϵ} and C_ϵ, we examine the "distance correlation" values[51] estimated based on the MCMC samples from their posterior distribution. The distance correlation is a measure of *dependence* between two random variables, being zero when they are independent. Given random variables X and Y with finite first moments, the distance correlation $\mathcal{R}(X,Y) \in [0,1]$ is defined as

$$\mathcal{R}(X,Y) = \frac{\vartheta^2(X,Y)}{\sqrt{\vartheta^2(X)\vartheta^2(Y)}} \tag{34}$$

where $\vartheta^2(X,Y)$ is the "distance covariance" between X and Y and $\vartheta^2(X)$ is the "distance variance," $\vartheta^2(X) = \vartheta^2(X,X)$. The distance covariance is given by

$$\begin{aligned}\vartheta^2(X,Y) =& E(||X-X'||||Y-Y'||)) \\ &+ E(||X-X'||)E(||Y-Y'||) \\ &- 2E(||X-X'||||Y-Y''||))\end{aligned}$$

where (X',Y'), (X'',Y'') are pairs of RVs with the same joint distribution as (X,Y), and $E(\cdot)$ denotes expectation.

Figure 10 shows the dependence of $\mathcal{R}(C_{\mu_\epsilon}, C_\epsilon)$ on the prior witdth for the two model parameters. For all model settings the distance correlation values between C_{μ_ϵ} and C_ϵ corresponding to the PEM approach is greater than approximately 0.6 indicating a relatively strong dependency between the two model parameters. For all filter sizes employed to filter the DNS data, these dependecies are largest when the prior is wide and decrease as the prior narrows and hence has a stronger effect on the posterior distributions. Since the priors for the two model constants are independent, this leads to weaker dependencies, i.e. smaller $\mathcal{R}(C_{\mu_\epsilon}, C_\epsilon)$ values. The results corresponding to the EEM approach are consistently smaller compared to the ones for the PEM approach. This observation is consistent with the less elongated posterior distributions for EEM compared to PEM, shown in Fig. 7 for select runs.

This last observation is not necessarily general when comparing PEM and EEM approaches. Due to its setup, i.e. embedding the error model in the physical model construction, the EEM approach will result in wider densities for the model parameters compared to the PEM approach. While we do not provide additional examples here, we believe that the degree of dependency between model parameters is case dependent and a general conclusion should not be drawn just based on the examples provided in this paper.

1. Posterior Predictive Distributions for Filtered DNS Data

In this section we explore the predictive skill of the k^{sgs} model given the posterior distributions for C_{μ_ϵ} and C_ϵ. We employ the Bayesian posterior predictive distribution[52] to determine the how well the model covers the filtered DNS data. This test examines the probability density of the predicted data, f_k^p, conditional on the existing data. Essentially it indicates how well the spread in the existing data is covered by the calibrated model. The marginal posterior distributions for the predicted $f_{k,i}$ at several times t_i corresponding to the original filtered DNS data is computed through

$$p^{pp}\left(f_{k,i}^p|\mathcal{D}\right) = \int_{f_{k,-i}} \left(\int_{C_{\mu_\epsilon},C_\epsilon} p(f_k^p|C_{\mu_\epsilon},C_\epsilon) p(C_{\mu_\epsilon},C_\epsilon|\mathcal{D}) dC_{\mu_\epsilon}\, dC_\epsilon \right) df_{k,-i}^p \tag{35}$$

Here, $p(f_k^p|C_{\mu_\epsilon},C_\epsilon)$ is the likelihood given by Eq. (19), $p(C_{\mu_\epsilon},C_\epsilon|\mathcal{D})$ is the posterior distribution for the model constants, and notation "$-i$" denotes all time locations, except i. Since the likelihood is constructed assuming independent errors between time locations, Eq. (35) simplifies to

$$p^{pp}\left(f_{k,i}^p|\mathcal{D}\right) = \int_{C_{\mu_\epsilon},C_\epsilon} p(f_{k,i}^p|C_{\mu_\epsilon},C_\epsilon) p(C_{\mu_\epsilon},C_\epsilon|\mathcal{D}) dC_{\mu_\epsilon}\, dC_\epsilon \tag{36}$$

For the PEM approach we will compare the posterior predictive distributions with the pushed-forward densities,

$$p^{pf}\left(f_{k,i}^p|\mathcal{D}\right) = \int_{C_{\mu_\epsilon},C_\epsilon} p(\mathcal{M}_i|C_{\mu_\epsilon},C_\epsilon) p(C_{\mu_\epsilon},C_\epsilon|\mathcal{D}) dC_{\mu_\epsilon}\, dC_\epsilon \tag{37}$$

Here, $\mathcal{M}_i \sim N(C_{\mu_\epsilon} f_{P,i} - C_\epsilon f_{D,i}, \sigma_{\mathcal{M}}^2)$, and σ_M is given by Eq. (18). The dependence on filter size Δ was omitted for brevity.

For the EEM approach the posterior predictive and the pushed-forward densities are the same. For this approach the error model is embedded in the posterior densities for the model parameters, hence the pushed-forward densities also represent a posterior predictive check.

Figure 11 shows a pushed-forward (PF), in dark grey, and posterior predictive (PP) densities, in light grey, for runs R3 and R4 using the PEM approach and just the posterior predictive density for the EEM approach (since it is the same as the pushed foward density in this case). Both the PF and the PP densities are illustrated via the 1-99% quantile ranges constructed from the corresponding densities. For the PEM approach, the PF $1-99\%$ quantile range, bordered by blue solid (R3) and dashed (R4) lines, is narrower than the spread observed in the filtered DNS data. This indicates that considering only the posterior densities of model parameters for further parametric studies will underestimate the full uncertainty established through the Bayesian framework presented here. In contrast, the PP $1-99\%$ quantile range, bordered by green lines for R3 and R4, covers well the spread observed in the filtered DNS data. Similar results are observed for the other runs. While this is encouraging, reproducing this approach is not feasible in practice as the error term is connected to a certain configuration, in this case the filtered DNS data. While posterior densities of model parameters can be carried to other configurations employing the same model, it is not clear how to estimate posterior predictictive distributions in configurations other than the one used for the calibration process. For the EEM approach this difficulty is circumvented by the fact that parameter densities are consistent with the data and there are no additional error terms involved. For this approach, the posterior $1-99\%$ quantile range, shown with red lines in Figure 11, is very close to the posterior predictive results for the PEM approach. Figure 12 shows further comparisons between PEM, with solid lines, and EEM, with dashed lines, for runs R1 and R5. For both these runs there is a similar agreement for the PP $1-99\%$ quantile range between the PEM and EEM approaches. Similar results are observed for runs R2 and R6 (results not shown).

2. Principal Component Analysis of Joint PDFs

Given the strong dependence in the joint posterior distribution of C_{μ_ϵ} and C_ϵ for PEM, we proceed with a Principal Component Analysis[53] (PCA) of these distributions. Through the PCA approach, we aim to identify linear combinations of these parameters that explain the MCMC samples. Let $X \in \mathbb{R}^{n\times 2}$ be a matrix with n rows and two columns, first column for C_{μ_ϵ} and second column for C_ϵ. Each row represents one MCMC sample. Without loss of generality, assume that the mean values are already subtracted from X.

The principal components (PC) of X are the eigenvectors of the covariance matrix $X^TX \in \mathbb{R}^{2\times 2}$, and the corresponding non-zero eigenvalues represent the variances of the MCMC data along the principal directions. For this study there are two principal directions corresponding to the parameter space spanned by C_{μ_ϵ} and C_ϵ. For the PEM approach, the PC analysis indicate that variances attributed to the 2^{nd} PC are less that 5% of the variances along the 1^{st} PC. This is consistent with the degree of dependency observed by visual inspection in Fig. 5 and by the distance correlation results in Fig. 10. For the EEM approach the variances along the 2^{nd} PC are about $10-15\%$ of the ones for the 1^{st} PC. This is consistent with the wider joint posterior distributions for C_{μ_ϵ} and C_ϵ for EEM compared to PEM.

In the next section, we will explore the dependency between C_{μ_ϵ} and C_ϵ along the 1^{st} PC for several cases. Figure 13 shows segments along the 1^{st} PC line corresponding to $R3_2$ corresponding to PEM and EEM, respectively. The ends of these segments correspond to the 5%-95% quantile range obtained from MCMC samples projected on the 1^{st} PC.

IV. FORWARD UQ

In this section we describe an approach for pushing forward the densities of model parameters $\theta = (C_{\mu_\epsilon}, C_\epsilon)$ and obtain probability densities for Quantities of Interest (QoIs) prediced by LES models. Figure 1 shows a schematic for the Forward UQ process in the bottom half. Below we provide a description of a non-intrusive approach, followed by a description of LES code and the configuration setup.

The non-intrusive propagation of uncertainty from model parameters θ to QoI y, proceeds through the following procedure. Given a basis of standard random variables $\boldsymbol{\xi} = (\xi_1, \xi_2, \ldots, \xi_n)$, and a known functional form $\theta = \theta(\boldsymbol{\xi})$, we employ the representation in Eq. (21) to cast the QoI y derived from the output of LES model f as a PCE expansion

$$y(\theta(\boldsymbol{\xi})) \approx \sum_{k=0}^{N_t} c_k \Psi_k(\xi_1, \xi_2, \ldots, \xi_n). \tag{38}$$

The coefficients of this PCE are evaluated by Galerkin projection exploiting the orthogonality of basis terms

$$c_k = \frac{\langle y\Psi_k\rangle}{\langle \Psi_k^2\rangle}. \tag{39}$$

Evaluation of the projection integrals in Eq. (39) require a number of evaluations of the model f. For small to moderate number of dimensions, numerical quadrature provides an efficient way to evaluate c_k using a number of samples much smaller compared to Monte Carlo sampling algorithms. The quadrature approach involves evaluating $y = f(\theta)$ for a particular set of parameter values $\theta^j = \theta(\xi_1^j, \xi_2^j, \ldots, \xi_n^j)$ corresponding to the set quadrature points required by the accuracy of the method. The PCE coefficients are then computed as

$$c_k = \frac{1}{\langle \Psi_k^2\rangle} \sum_{j=1}^{N_q} w_j f(\theta^j) \tag{40}$$

where, w_j is the weight corresponding to the quadrature point $\theta^j = \theta(\xi_1^j, \ldots, \xi_n^j)$, and N_q is the number of quadrature points.

Once the PCE is constructed for QoI y, moments of the distribution of y can be estimated analytically based on the expansion coefficients c_k.[38] For example the expectation of y is given by c_0. The PCE in Eq (38) can also be used as a "surrogate" when the computational model is expensive and/or the probability density of the input parameters are updated. For example the probability density of y can be evaluated with negligible cost compared to the full model evaluations. In the following sections we describe the setup for the LES simulations, followed by additional manipulation of the input parameter space to help construct PCE for several QoIs.

A. Channel Flow Setup

In this section we describe the LES model f, employed to propagate densities from model parameters to output QoIs. For this study, the model f, referenced in Fig. 1, is represented by the SIERRA Thermal/Fluids software, developed by Sandia National Labs. It is designed to simulate turbulent reacting flow and heat transfer[54] on massively parallel computers, and was built on the SIERRA framework.[55] In this work the low-Mach number module is used. The discretization scheme is based on the control volume finite element method[56] where the partial differential equations of mass, momentum, and energy are integrated over unstructured control volumes. The one equation subgrid-scale kinetic turbulent energy model[46,57] as calibrated in the first part of this study was used for this forward UQ propagation considering a different geometry of a parallel plane channel flow at a Reynolds number of $\mathrm{Re}_\tau = 590$. This value was chosen to match the Direct Numerical Simulation (DNS) work done by Moser *et.al.*[58]

The channel dimensions are $2\pi h \times 2h \times \pi h$ in the streamwise, wall-normal, and spanwise directions, respectively. The boundary conditions are periodic in both the streamwise and spanwise directions, and no slip walls are applied at both the top and bottom boundaries. There are 48 uniformly spaced grid nodes in both streamwise and spanwise directions. In the wall normal direction there are 103 nodes, with the first four nodes from the walls placed uniformly with a $y^+ = 1$ spacing. The grid is then stretched through a hyperbolic tangent function until the spacing at the centerline is approximately equal to the spacing in the spanwise direction. We note that our grid setup is considerably more coarse than the fully resolved DNS case for a $Re_\tau = 590$ presented by Moser *et.al.*[58] in which the number of nodes were $383 \times 257 \times 383$ in the streamwise, wall normal, and spanwise directions respectively. We employ a CFL number of about 0.5, resulting in a time step of approximately 10^{-4}. The time coordinate is normalized by the channel half-width h.

B. Rosenblatt Transformation

In order to construct the PCE presented in Eq. (38) we map the parameter space θ that employs dependent densities for its components to the ξ space where all coordinates have independent densities. For this study, the θ space consists of $(C_{\mu_\epsilon}, C_\epsilon)$, the ξ space consists of (ξ_1, ξ_2), and the map between the two can be constructed via the Rosenblatt transformation.[59] The inverse of the Rosenblatt transformation can formally be written as

$$\begin{aligned} C_{\mu_\epsilon} &= \tilde{F}^{-1}_{C_{\mu_\epsilon}}(\xi_1), \\ C_\epsilon &= \tilde{F}^{-1}_{C_\epsilon | C_{\mu_\epsilon}}(\xi_2 | \xi_1), \end{aligned} \tag{41}$$

where ξ_1, ξ_2 are i.i.d. uniform random variables. Eq. (41) relates the regular, *mapped* domain $[0,1] \times [0,1]$ to the pair $(C_{\mu_\epsilon}, C_\epsilon)$ and uses the inverses of the marginal, $\tilde{F}^{-1}_{C_{\mu_\epsilon}}$, and conditional, $\tilde{F}^{-1}_{C_\epsilon | C_{\mu_\epsilon}}$, cumulative distribution functions (CDF) for the random variable pair $(C_{\mu_\epsilon}, C_\epsilon)$.

Numerically, the Rosenblatt transformation is computed through interpolation tables constructed for the CDF functions in Eq. (41). To illustrate this approach we use the joint density for the uncertain parameters C_{μ_ϵ} and C_ϵ, corresponding to an average of the joint posterior distribution for runs R3 and R4 via the EEM approach. This ensures that LES runs cover a region wide enough in the parameter space, leading to a PCE that can be used as a surrogate to push forward the joint distributions for C_{μ_ϵ} and C_ϵ corresponding to all runs R3 and R4.

Figure 14 shows the correspondence between physical parameter space $(C_{\mu_\epsilon}, C_\epsilon)$ and the space parameterized by uniform random variables (ξ_1, ξ_2). The markers show the location of quadrature points corresponding to a Gauss-Legendre quadrature approach. Their images in the physical space are mostly distributed around the regions where the joint density $p(C_{\mu_\epsilon}, C_\epsilon)$ is significant.

C. Polynomial Chaos Expansions

We performed a set of LES simulations using the setup for the channel flow described in Section IV A. Each simulation corresponds to C_{μ_ϵ} and C_ϵ values selected according to the Rosenblatt transform presented in Section IV B. Using the raw LES data, we computed several QoIs. Specifically, we estimated the centerline velocity, $\overline{u}$, the maximum velocity RMS, $\overline{u}_{RMS}$, and the mass flux, $\overline{\dot{m}}$. All these QoIs are averaged in time over approximately five flow-through times. Using the discrete values for these QoIs we then estimate the coefficients of their corresponding PCE via the quadrature approach presented in Eq. (40).

The mean centerline velocity, in Fig. 15a, exhibits a quasi-linear trend in the ξ_1 direction and a weak quadratic trend in ξ_2. The mean values of the peak axial velocity RMS, in Fig. 15b, exhibit a quadratic dependency on the input parameters while the mean mass flux,

in Fig. 15c, shows a shape similar to the mean centerline velocity. For this work the ξ_1 coordinate is mostly aligned with the first principal component of $(C_{\mu_\epsilon}, C_\epsilon)$, while ξ_2 is proportional to C_ϵ.

We examined the relative L_2 error between LES simulations and the PCE values for these QoIs. These errors are around 6% for $\overline{u}$ and $\overline{\dot{m}}$, and less than 10% for $\overline{u}_{RMS}$. While, in principle, longer time averages can reduce the noise in the LES values and allow lower discrepancies compared to the corresponding PCEs, we consider these errors to be reasonable for the subsequent use of the PCEs as surrogate models.

D. Probability Densities for Quantities of Interest

We employ the PCEs discussed in the previous section to compute values for several QoIs using the MCMC samples for C_{μ_ϵ} and C_ϵ corresponding to several runs and conditions discussed in Section III. The resulting PCE-approximated model evaluations are then used to compute the PDFs of the output QoIs via KDE. This procedure is repeated for all calibration studies shown in Table I.

Figure 16a shows the densities for the mean centerline velocity $\overline{u}$ for R3 corresponding to several filter widths. The results in this figure indicate a strong effect exercised by the filter size, on the PDF of$\overline{u}$. The parameter densities corresponding to smaller filter widths, i.e. $\Delta = L/64$ (red lines), shift the center of mass to higher velocity values. Larger filter widths shift the most likely values for the centerline velocities towards smaller values which are closer to the DNS value. Earlier DNS results[58] indicate a reference value of 21.26 for the mean centerline velocity. We attribute the discrepancy between the DNS value and our LES study to other sources of error that can impact this configuration such as insuficient grid resolution, in particular near the walls.

The wider PDFs observed for $(C_{\mu_\epsilon}, C_\epsilon)$ with the EEM approach translate into wider PDF's for the mean centerline velocity compared to PEM values. This is consistently observed for all filter widths. Results corresponding to other runs are qualitatively similar to the ones observed for R3. Both the peak RMS of the axial velocity, in Fig. 15b, and the mass flux, in Fig. 15c, show output densities that are qualitatively similar to results for the centerline velocity.

Next we compare the posterior densities obtained by sampling the full joint PDFs of C_{μ_ϵ} and C_ϵ with the posterior PDFs obtained by sampling the density along the corresponding 1^{st} PCs. The results shown in Fig. 17 correspond to $R3_2$. For the PEM approach the the results based on the densities along the 1^{st} PC, with dashed red line, are in close agreement with the results based on full joint PDFs with solid red line. This indicates that, for this particular study, the strong dependency between the two input parameters for PEM effectively renders the output being dependent only on the linear combination of the two parameters. Unlike for PEM, the EEM results show a significant discrepancy between the full joint posterior and the values based on the 1D density along the 1^{st} PC. For this set of cases the width of the joint posterior is important to the system behavior and reduced dimensionality data do not capture the full range of results. The PCA-based results for other runs and QoIs are qualitatively similar to the ones observed in Fig. 17.

V. CONCLUSIONS

In this paper we present a Bayesian framework for estimating joint densities for LES turbulent sub-grid scale model parameters based on filtered DNS data. These densities are then propagated forward through LES of channel flow to generate probability densities for several quantities of interest.

We employ DNS of forced isotropic turbulence, downloaded from the Johns Hopkins Turbulence Database, to calibrate two parameters for the sub-grid scale turbulent kinetic energy model employed in LES. We employ Gaussian priors for the model parameters, centered at values previously reported in the literature for these parameters. We then explore the effect of prior widths on the posterior densities and several summary statistics of interest. In this context we compare two approaches for treating the discrepancy between the model and the data in the Bayesian framework. In the first approach, abbreviated as PEM, the discrepancy is presumed Gaussian with zero mean, and the standard deviation is inferred together with the posterior densities for the model parameters. In the second approach, developed recently by some of the co-authors of this paper and abbreviated as EEM, the error is embedded in the formulation of the model parameters.

We find that the filter size, employed to filter the DNS data, has a significant impact on the posterior means for the model parameters, while the effect on the marginal posterior standard deviations is weaker. We also observe that prior widths affect mostly marginal posterior standard deviations, while the priors means are less important for the posterior means. We find that the EEM approach leads to wider joint densities for the model parameters compared to the PEM approach. This also results in weaker dependencies between the two model parameters for EEM, while for PEM, these dependencies are very strong.

In the second part of the paper, the joint posterior densites for the LES model parameters are propagated forward to several quantities of interest (QoI). We employ a non-intrusive approach, and construct Polynomial Chaos expansions (PCEs) for these QoIs. The expansion coefficients are estimated via Galerkin projection. Specifically, the projection integrals are computed via Gauss-Legendre quadrature. Twenty-five LES channel flow simulations were run with the two model constants set ac-

cording to the corresponding quadruature points. Once the coefficients of these PCEs were available, the densities for the corresponding QoIs were evaluated through multiple samples of the PCEs. We found that the first pricipal component corresponding to the joint posterior density leads to forward UQ results that are very close to the ones based on the full densities in the PEM approach which show narrow joint posterior densities. Unlike the PEM approach, EEM leads to wider posterior densities, possibly accounting for model error and the first principal component is no longer sufficient to explain the dependence on the input parameters.

The use of informative priors was necessary to constrain the parameter space as the isotropic turbulence data was sufficient to constrain the ratio between the model parameters considered here, but not their values. It is suggested that in the future this calibration process use data from multiple complementary flows to better estimate all unknowns. Even in this case it is likely that the filter width will play a significant role in the resulting model form despite the fact that many turbulence models, such as this one, include a parameterized dependence on the filter width. It will also be important to match the filter width when propagating these uncertain turbulence models through a flow as this work provides data showing the impact of filter width on important flow quantities.

ACKNOWLEDGMENTS

This work was funded by the Laboratory Directed Research & Development (LDRD) program at Sandia National Laboratories. Sandia National Laboratories is a multiprogram laboratory operated by Sandia Corporation, a wholly owned subsidiary of Lockheed Martin Corporation, for the United States Department of Energy's National Nuclear Security Administration under contract DE-AC04-94AL85000.

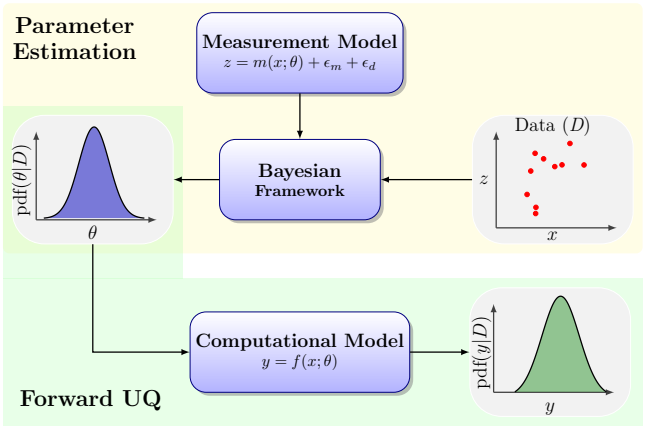

FIG. 1: Schematic of parameter estimation and forward UQ workflows.

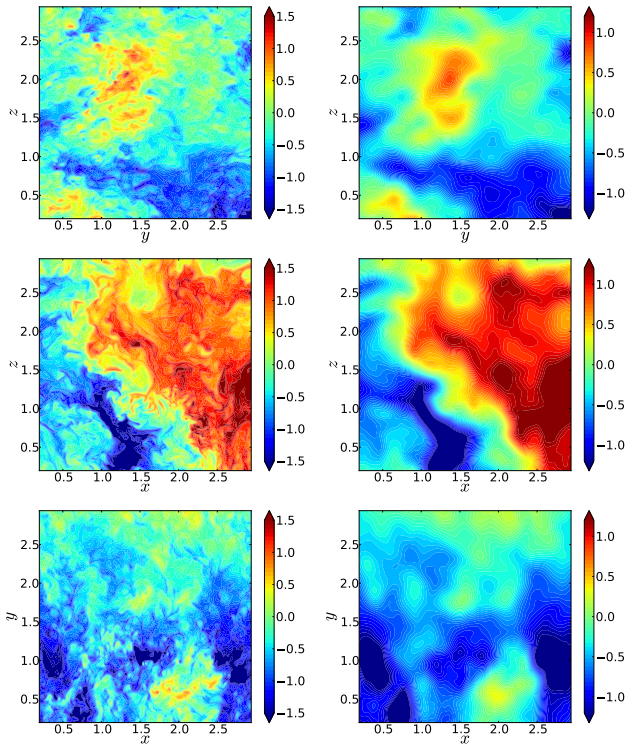

FIG. 2: Snapshot of$u$, v, and w velocity components: DNS data (left column) and filtered date (right column) at $t = 0.4$ for a filter size $\Delta = L/32$.

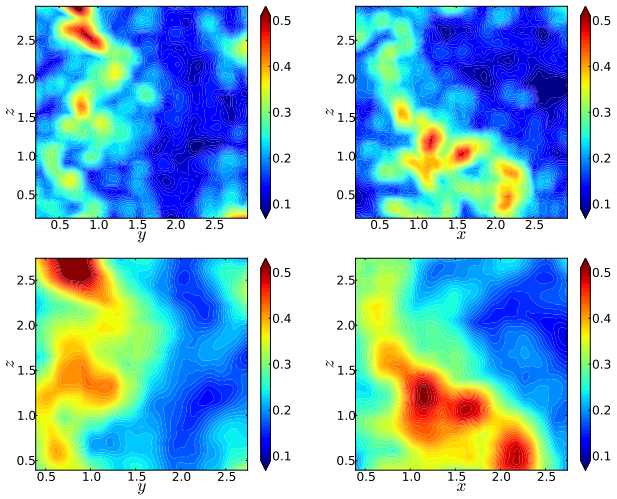

FIG. 3: Snapshots of $\sqrt{k^{sgs}}$ field at $t = 0.4$ for filter sizes $\Delta = L/32$ (top row) and $\Delta = L/16$ (bottom row).

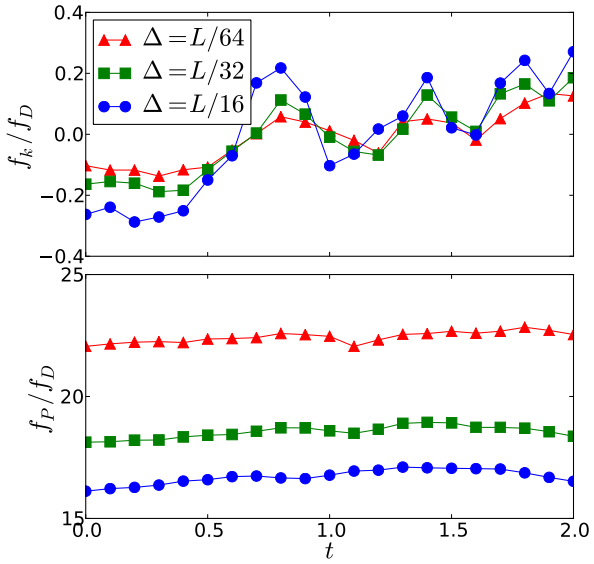

FIG. 4: Time evolution for f_k/f_D (top frame) and f_P/f_D (bottom frame) for several filter sizes Δ.

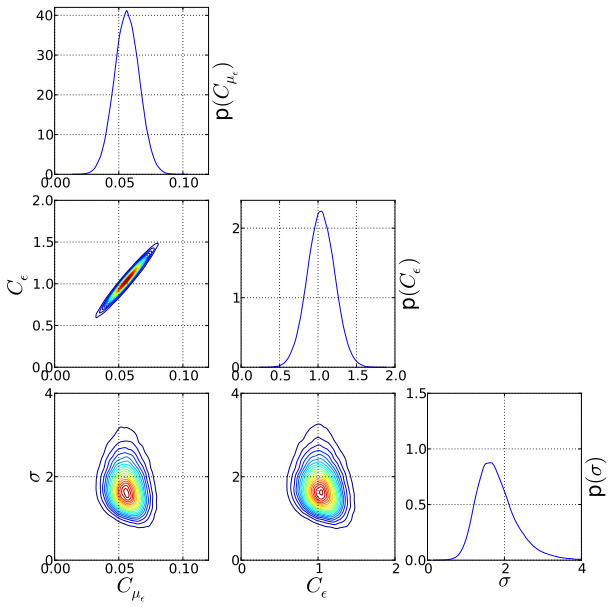

FIG. 5: Joint posterior distribution for model parameters corresponding to $R3_2$ using PEM. For this case the filtered DNS data employed a filter size $\Delta = L/32$ and the prior densities were centered at $\mu_1^{pr} = (0.0845, 0.85)$ with marginal standard deviations $\sigma_2^{pr} = (0.02, 0.2)$.

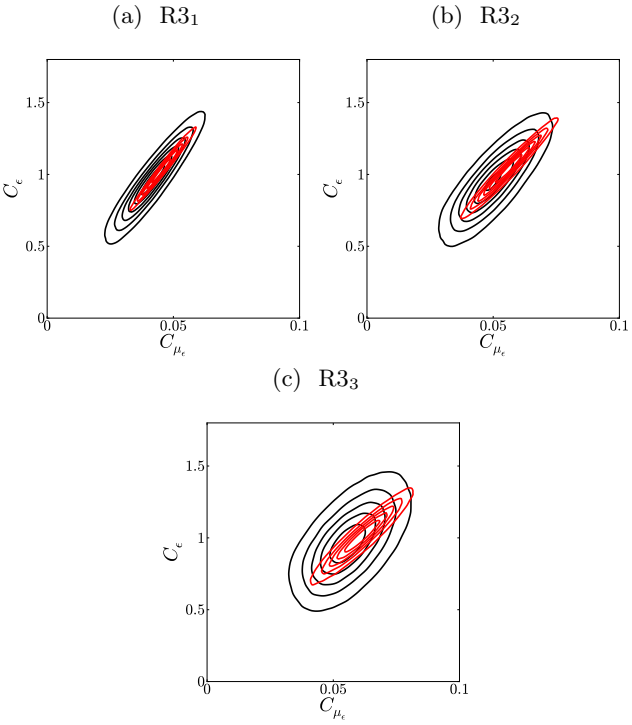

FIG. 7: Comparison of joint posterior distribution for $(C_{\mu_\epsilon}, C_\epsilon)$, for PEM (red contours) and EEM (black contours).

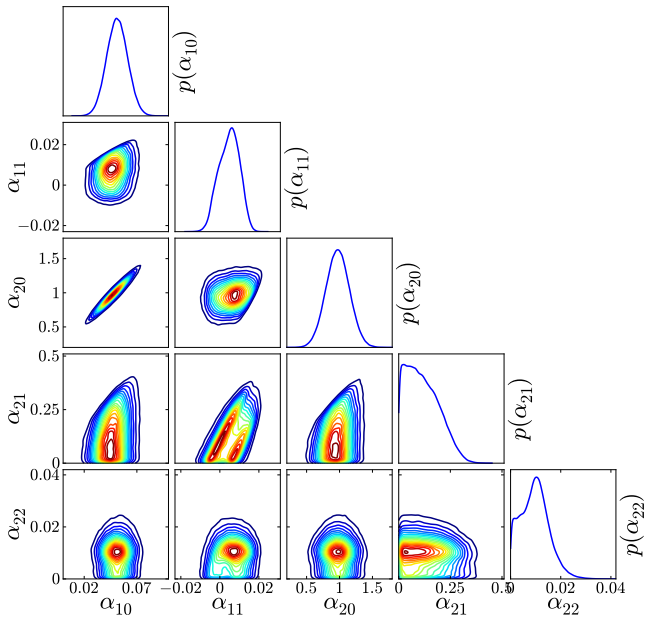

FIG. 6: Joint posterior distribution for EEM parameters α_{ij}, corresponding to $R3_2$.

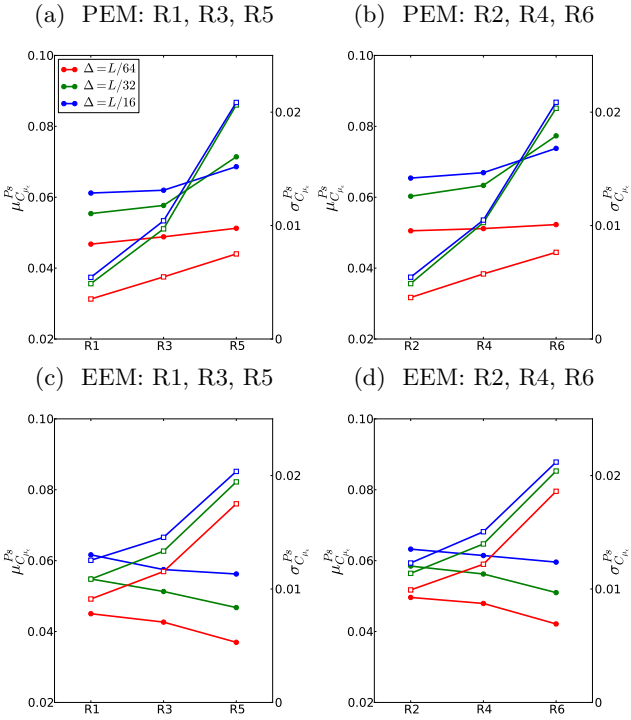

FIG. 8: Posterior mean (left axis, filled circles) and standard deviation (right axis, white squares) for C_{μ_ϵ}.

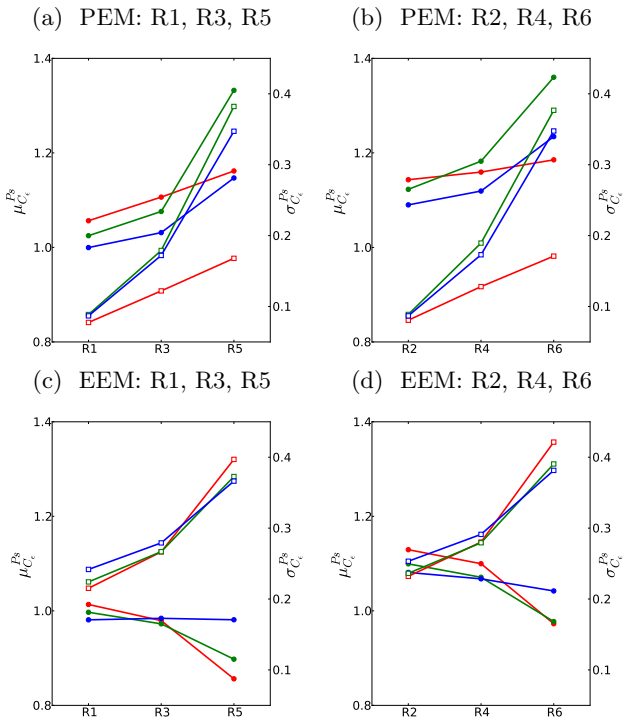

FIG. 9: Posterior mean (left axis, filled circle) and standard deviation (right axis, white square) for C_ϵ. The color scheme is the same as in Fig. 8.

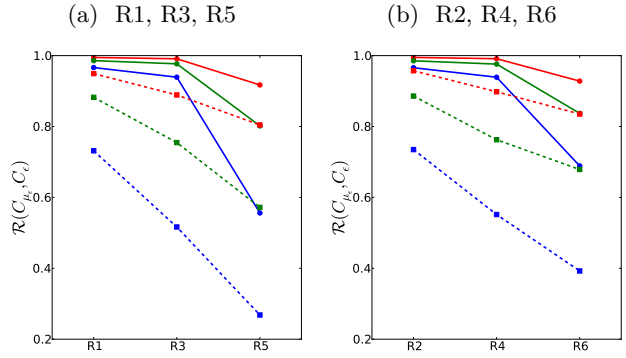

FIG. 10: Distance correlation dependency on the standard deviation of the marginal prior densities of C_{μ_ϵ} and C_ϵ via PEM (solid lines) and EEM (dashed lines). The color scheme corresponds to several filter sizes, and is the same as in Fig. 8.

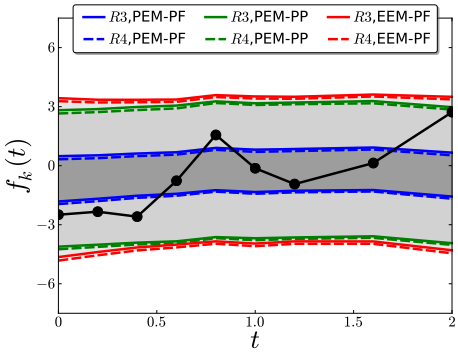

FIG. 11: Push-forward (PF) and posterior predictive (PP) $1-99\%$ quantile ranges for runs R3 (solid lines) and R4 (dashed lines). The filtered DNS data is shown with black lines and circles.

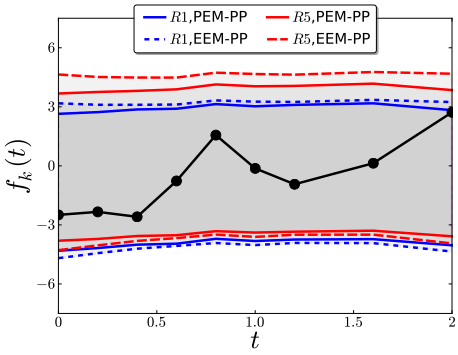

FIG. 12: Posterior predictive $1-99\%$ quantile ranges PEM (solid lines) and EEM (dashed lines). The filtered DNS data is shown with black lines and circles.

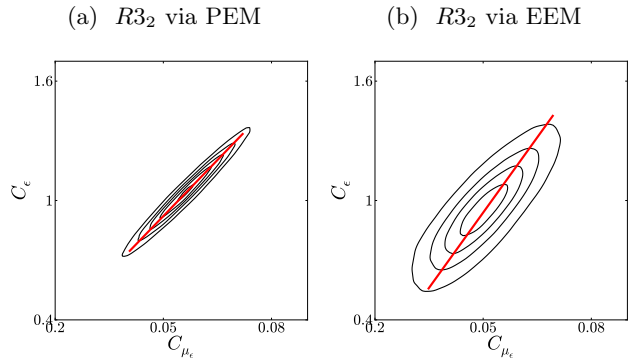

FIG. 13: Joint posterior distribution via PEM (left frame) and EEM (right frame) for $R3_2$. The red segments show the first principal component computed from MCMC samples. The ends of each segment correspond to the 5%-95% quantile range for MCMC samples projected on the 1st principal component.

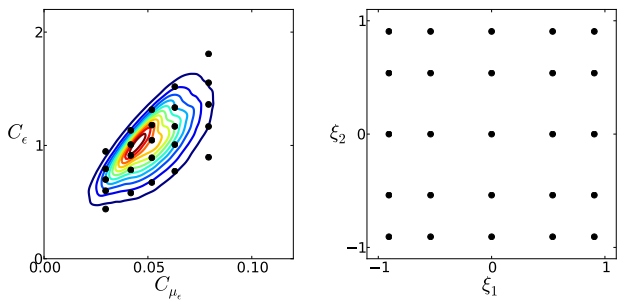

FIG. 14: Illustration of the correspondence between samples in the parameter space and their images via the Rosenblatt map to the space parameterized by (ξ_1, ξ_2).

(a) Mean Centerline Velocity, $\overline{u}$ (21.26)

(b) Mean Velocity RMS, $\overline{u_{RMS}}$ (2.74)

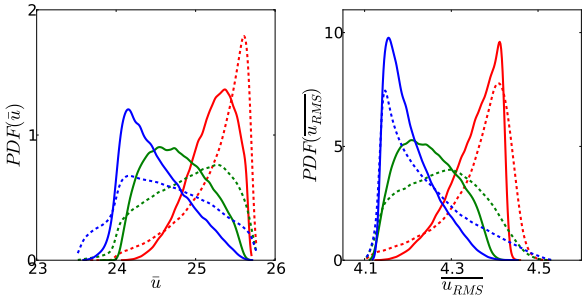

(c) Mean Mass Flux, $\overline{\dot{m}}$ (117.2)

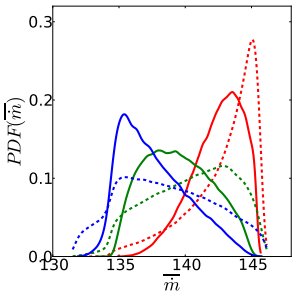

FIG. 16: PDF's for several quantities of interest corresponding to LES results in a channel flow configuration. Red, green, and blue correspond to filter widths $\Delta = \{L/64, L/32, L/16\}$ for R3. Solid lines show pushed forward PDF's for the PEM approach while dashed show EEM results. The DNS values[58] are shown in parantheses in the corresponding captions.

(a) Axial Velocity on the Centerline

(b) Peak Axial Velocity RMS

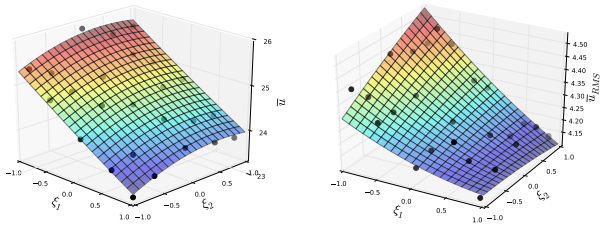

(c) Mass Flux

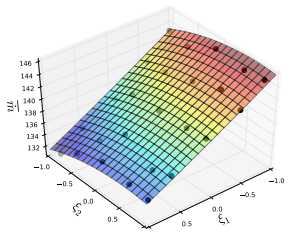

FIG. 15: Polynomial Chaos expansions several QoI as a function of (ξ_1, ξ_2).

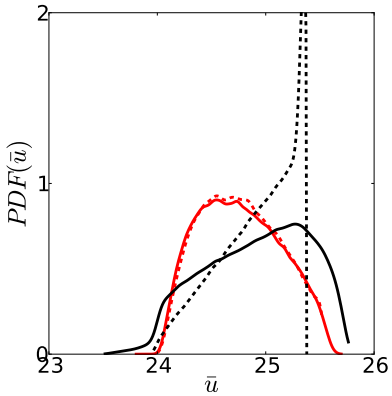

FIG. 17: Output PDFs for mean centerline velocity based on forward propagation of the joint PDFs of C_{μ_ϵ} and C_ϵ (solid lines) and the joint density along the 1st PC (dashed lines). Results corresonding to $R3_2$, PEM results shown in red and EEM in black.

[1]P. Sagaut, *Large Eddy Simulation for Incompressible Flows* (Springer, 2005).
[2]C. Kaul and V. Raman, Physics of Fluids **23**, 035102 (2011).
[3]J. Meyers, B. Geurts, and M. Baelmans, Physics of Fluids **15**, 2740 (2003).
[4]J. Gullbrand and F. Chow, Journal of Fluid Mechanics **495**, 323 (2003).
[5]S. Bose, P. Moin, and D. You, Physics of Fluids **22**, 105103 (2010).
[6]R. Moser, N. Malaya, H. Chang, P. Zandonade, V. P., A. Bhattacharya, and A. Haselbacher, Physics of Fluids **21**, 105104 (2009).
[7]S. Völker, R. Moser, and P. Venugopal, Physics of Fluids **14**, 3675 (2002).
[8]J. Templeton and M. Shoeybi, Multiscale Modeling and Simulation **5**, 420 (2006).
[9]J. Borggaard and T. Iliescu, Applied Mathematics Letters **19**, 735 (2006).
[10]M. Shoeybi and J. Templeton, in *Center for Turbulence Research Annual Research Briefs* (2006).
[11]A. Bhattacharya, A. Das, and R. Moser, Physics of Fluids **20**, 115104 (2008).
[12]F. Rizzi, M. Salloum, Y. Marzouk, R. Xu, M. Falk, T. Weihs, G. Fritz, and O. Knio, Multiscale Modeling and Simulation **10**, 550 (2011).
[13]M. Salloum and J. Templeton, International Journal for Uncertainty Quantification **4**, 171 (2014).
[14]M. Christie, V. Demyanov, and D. Erbas, Journal of Computational Physics **217**, 143 (2006).
[15]A. Fox, M. Williams, A. D. Richardson, D. Cameron, J. H. Gove, T. Quaife, D. Ricciuto, M. Reichstein, E. Tomelleri, C. M. Trudinger, and M. T. V. Wijk, Agricultural and Forest Meteorology **149**, 1597 (2009).
[16]D. M. Ricciuto, A. W. King, D. Dragoni, and W. M. Post, Journal of Geophysical Research: Biogeosciences **116** (2011), 10.1029/2010JG001400.
[17]S. Cheung, T. Oliver, E. Prudencio, S. Prudhomme, and R. Moser, Reliability Engineering and System Safety **96**, 1137 (2011).
[18]T. Oliver and R. Moser, Physics of Fluids **318**, 042032 (2011).
[19]T. Oliver and R. Moser, Physics of Fluids **24**, 075108 (2012).
[20]M. Emory, J. Larsson, and G. Iaccarino, Physics of Fluids **25**, 110822 (2013).
[21]P. Pettersson, G. Iaccarino, and J. Nordström, Journal of Computational Physics **228**, 8394 (2009).
[22]P. Pettersson, J. Nordström, and G. Iaccarino, Acta Mathematica Scientia **30B**, 539 (2010).
[23]P. Congedo, C. Duprat, G. Balarac, and C. Corre, International Journal for Numerical Methods in Fluids **72**, 341 (2012).
[24]M. Reagan, H. Najm, R. Ghanem, and O. Knio, Combustion and Flame **132**, 545 (2003).
[25]D. Lucor, J. Meyers, and P. Sagaut, Journal of Fluid Mechanics **585**, 255 (2007).
[26]J. Ling, F. Coletti, S. Yapa, and J. Eaton, International Journal of Heat and Fluid Flow **44**, 348 (2013).
[27]K. Sargsyan, H. N. Najm, and R. Ghanem, in preparation (2014).
[28]H. Najm, Annual Review of Fluid Mechanics **41**, 35 (2009).
[29]K. Duraisamy and P. Chadrashekar, Computers and Fluids **66**, 10 (2012).
[30]Q. Wang, K. Duraisamy, J. Alonso, and G. Iaccarino, AIAA Journal **50**, 581 (2012).
[31]R. Adrian, "Stochastic estimation of the structure of turbulent fields," Tech. Rep. TAM Report No. 800, UILU-ENG-95-6022 (Theoretical and Applied Mechanics, University of Illinois, 1995).
[32]http://www.sandia.gov/UQToolkit UQTk v3.0 is currently undergoing formal review. In the meantime, the source code is available upon request from Bert Debusschere (bjdebus@sandia.gov).
[33]A. Yoshizawa, Physics of Fluids (1958-1988) **29**, 2152 (1986).
[34]A. Yoshizawa, Phys. Rev. E **48**, 273 (1993).
[35]E. Perlman, R. Burns, Y. Li, and C. Meneveau, in *Supercomputing, 2007. SC '07. Proceedings of the 2007 ACM/IEEE Conference on* (2007) pp. 1–11.
[36]Y. Li, E. Perlman, M. Wan, Y. Yang, C. Meneveau, R. Burns, S. Chen, A. Szalay, and G. Eyink, Journal of Turbulence **9**, 1 (2008).
[37]L. M. Berliner, J. Geophys. Res. **108**, 8776 (2003).
[38]R. Ghanem and P. Spanos, *Stochastic Finite Elements: A Spectral Approach* (Springer Verlag, New York, 1991).
[39]B. Debusschere, H. Najm, P. Pébay, O. Knio, R. Ghanem, and O. Le Maître, SIAM Journal on Scientific Computing **26**, 698 (2004).
[40]N. Wiener, Am. J. Math. **60**, 897 (1938).
[41]S. Janson, *Gaussian Hilbert Spaces* (Camb. Univ. Press, Cambridge, UK, 1997).
[42]D. Xiu and G. Karniadakis, SIAM Journal on Scientific Computing **24**, 619 (2002).
[43]R. Askey and J. Wilson, Memoirs Amer. Math. Soc. **319**, 1 (1985).
[44]B. Silverman, *Density Estimation for Statistics and Data Analysis* (Chapman and Hall, London, 1986) pp. 75–94.
[45]D. Scott, *Multivariate Density Estimation. Theory, Practice and Visualization* (Wiley, New York, 1992) pp. 125–194.
[46]U. Schumann, Theoretical and Computational Fluid Dynamics **2**, 279 (1991).
[47]W. R. Gilks, S. Richardson, and D. J. Spiegelhalter, *Markov Chain Monte Carlo in Practice* (Chapman & Hall, London, 1996).
[48]H. Haario, E. Saksman, and J. Tamminen, Bernoulli **7**, 223 (2001).
[49]A. Raftery and S. Lewis, in *Bayesian Statistics 4* (Oxford University Press, 1992) pp. 763–773.
[50]R. Kass, B. Carlin, A. Gelman, and R. Neal, The American Statistician **52**, 93 (1998).
[51]G. Székely, M. Rizzo, and N. Bakirov, Annals of Statistics **35**, 2769 (2007).
[52]S. Lynch and B. Western, Sociological Methods and Research **32**, 301 (2004).
[53]I. T. Jolliffe, *Principal Component Analysis* (Springer, 2002).
[54]C. D. Moen, G. H. Evans, S. P. Domino, and S. P. Burns, in *ASME 2002 International Mechanical Engineering Congress and Exposition*, Vol. 6 (ASME, 2002) pp. 25–32.
[55]J. Stewart and H. Edwards, in *Large-Scale PDE-Constrained Optimization*, Lecture Notes in Computational Science and Engineering, Vol. 30, edited by L. T. Biegler, M. Heinkenschloss, O. Ghattas, and B. van Bloemen Waanders (Springer Berlin Heidelberg, 2003) pp. 301–315.
[56]W. J. Minkowycz, E. M. Sparrow, G. E. Schneider, and R. H. Pletcher, *Handbook of Numerical Heat Transfer* (Wiley-Interscience, 1988).
[57]U. Schumann, Journal of Computational Physics **18**, 376 (1975).
[58]R. D. Moser, J. Kim, and N. N. Mansour, Physics of Fluids **11**, 943 (1999).
[59]M. Rosenblatt, Annals of Mathematical Statistics **23**, 470 (1952).